JACS
JOURNAL OF THE AMERICAN CHEMICAL SOCIETY

Article

pubs.acs.org/JACS

Evidence of Charge-Transfer Ferromagnetism in Transparent Diluted Magnetic Oxide Nanocrystals: Switching the Mechanism of Magnetic Interactions

Shokouh S. Farvid,‡ Tahereh Sabergharesou,‡ Lisa N. Hutfluss, Manu Hegde, Eric Prouzet, and Pavle V. Radovanovic*

Department of Chemistry, University of Waterloo, 200 University Avenue West, Waterloo, Ontario N2L 3G1, Canada

Supporting Information

ABSTRACT: We report the experimental evidence of a new form of room-temperature ferromagnetism in high surface area nanocrystalline manganese-doped In_2O_3, prepared from colloidal nanocrystals as building blocks. The nanocrystal structure (bixbyite or corundum) and assembly were controlled by their size, and the type and concentration of dopant precursors. The existence of substitutional paramagnetic Mn dopant ions in mixed valence states (Mn^{2+} and Mn^{3+}) was confirmed and quantified by different spectroscopic methods, including X-ray absorption and magnetic circular dichroism. The presence of different oxidation states is the basis of ferromagnetism induced by Stoner splitting of the local density of states associated with extended structural defects, due to charge transfer from the Mn dopants. The extent of this charge transfer can be controlled by the relationship between the electronic structures of the nanocrystal host lattice and dopant ions, rendering a higher magnetic moment in bixbyite relative to corundum Mn-doped In_2O_3. Charge-transfer ferromagnetism assumes no essential role of dopant as a carrier of the magnetic moment, which was directly confirmed by X-ray magnetic circular dichroism, as an element-specific probe of the origin of ferromagnetism. At doping concentrations approaching the percolation limit, charge-transfer ferromagnetism can switch to a double exchange mechanism, given the mixed oxidation states of Mn dopants. The results of this work enable the investigations of the new mechanisms of magnetic ordering in solid state and contribute to the design of new unconventional magnetic and multifunctional materials.

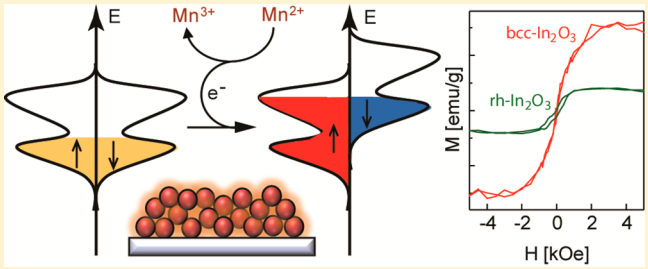

INTRODUCTION

The synergy of different electronic properties of solid state materials is the basis for various phenomena of fundamental and practical importance.[1] Specifically, the interactions of electron charge and spin degrees of freedom are at the core of the rapidly emerging field of spintronics, which relies on using electron spin states, alone or in addition to charge, for information processing, transmittal, and storage.[2] Diluted magnetic semiconductors (DMSs)[3] have attracted much interest for application in spintronics because they can spontaneously generate polarized spins, which could then be electrically injected into nonmagnetic semiconductors,[4] leading to new classes of electronic and photonic devices, such as spin transistors and lasers.[5] Spin polarization in DMSs is enabled by exchange interactions between unpaired d electrons on transition metal impurities and the host lattice band structure electrons. Practical implementation of DMSs in spintronic technologies requires the design and preparation of transition-metal-doped semiconductors in which ferromagnetic ordering of dopant centers can be achieved at or above room temperature. The design and preparation of DMSs in nanostructured form has proven to be a promising route in this regard. It has already been demonstrated that generation of multiple electrons by photoexcitation of colloidal DMS nanocrystals (NCs) can facilitate robust electron-mediated ferromagnetic interactions at room temperature.[6] Such multiple carrier occupancy may also lead to other unusual magnetic phenomena, such as closed-shell magnetism and imprinting of carrier correlation on magnetic dopants.[7]

Among the semiconductor host lattices explored, wide band gap metal oxides have been particularly intriguing, owing to the early reports of high Curie temperature (T_C) ferromagnetism in Co-doped TiO_2 and ZnO.[8−10] These oxides may also exhibit other unique properties, including polymorphism, transparency, conductivity, and photoluminescence, and are often generally referred to as transparent conducting oxides (TCOs).[11,12] However, the concentration of dopant ions in diluted magnetic semiconductor oxides (DMSOs) exhibiting high T_C ferromagnetism is usually below the percolation limit, and the long-range ordering cannot be readily explained by traditional mechanisms of magnetic interactions in oxides, including double exchange or superexchange. Furthermore, the electronic structure of TCO host lattices and the concentration and type

Received: February 22, 2014
Published: May 16, 2014

   dx.doi.org/10.1021/ja501888a | J. Am. Chem. Soc. 2014, 136, 7669−7679

of charge carriers may not always be compatible with carrier-mediated long-range magnetic ordering or bound magnetic polaron formation. Elucidating the mechanism of magnetic interactions in DMSOs has emerged as one of the most challenging problems in the field of magnetism, and diluted magnetic oxides have in many ways become a proxy for the general understanding of dilute ferromagnetism as a new form of magnetic interactions in solid state.[13]

Significant insight into the origin of magnetism in DMSOs has been obtained by in situ preparation and studies of transition-metal-doped TCO nanostructures.[9,14−16] The investigations of colloidal DMSO NCs have suggested the role of extended interfacial defects in mediating long-range magnetic ordering.[9,16−18] While free-standing NCs are found to be largely paramagnetic, the nanocrystalline films prepared from colloidal NCs as building blocks exhibit ferromagnetism, presumably owing to the high concentration of oxygen vacancies associated with the grain boundaries formed by contacting NCs.[18] It has been proposed that these oxygen vacancies form a shallow donor band, which can hybridize with unoccupied d electrons on transition metal dopants at the Fermi level, mediating their ferromagnetic exchange interactions and leading to the creation of bound magnetic polarons.[19] This model has subsequently been expanded and generalized to account for the observation of ferromagnetism in DMSO systems involving acceptor states.[20] However, in several studies ferromagnetism has also been reported for nanocrystalline oxides that nominally contain no magnetic impurities,[21] or DMSOs in which magnetic dopants remain in the paramagnetic form,[22] indicating that other mechanisms of ferromagnetism in nanostructured materials may also be possible. Experimental investigation of the proposed models, as well as other possible mechanisms of ferromagnetic interactions in DMSOs, requires the design and synthesis of transition-metal-doped TCOs with a tunable electronic structure of the dopant ion and the host lattice. We have recently shown that the structure of In_2O_3 NCs can be manipulated by controlling NC size via growth kinetics and the concentration of dopant impurities in the reaction mixture.[12,23] These phenomena allowed for the stabilization of In_2O_3 NCs in bixbyite phase having a body-centered cubic unit cell structure (bcc-In_2O_3) or corundum phase having rhombohedral structure (rh-In_2O_3). Manganese(III) is a moderately oxidizing ion,[24] allowing for the possibility of controlling dopant oxidation state in Mn-doped In_2O_3 (Mn:In_2O_3) NCs. Changing the oxidation state could be a vehicle for manipulating the d orbital-derived states with respect to the host lattice band structure and the native defect states.

Relative to other TCO systems, In_2O_3-based DMSO NCs have been much less explored,[14−17] and in particular, there has been no report on the synthesis and investigation of Mn-doped rh-In_2O_3 (Mn:rh-In_2O_3). Stabilization of rh-In_2O_3 in bulk generally requires high pressure or temperature,[25] which can lead to expulsion of the dopant ions, or secondary phase formation. Similarly to other DMSO NCs, conflicting observations have been reported for Mn-doped bcc-In_2O_3 (Mn:bcc-In_2O_3). The samples, having nominally the same composition, are shown to exhibit different magnetic properties if prepared by different methods or under different conditions. While early study has shown that bulk Mn:bcc-In_2O_3 is intrinsically paramagnetic for low doping concentrations,[26] in subsequent investigations room-temperature ferromagnetism has also been observed.[27] Here we show that Mn dopant ions exhibit mixed oxidation states (Mn^{2+} and Mn^{3+}) and are paramagnetic in both bcc- and rh-In_2O_3 NCs. On the other hand, nanocrystalline films prepared from colloidal NCs turn ferromagnetic, with the net magnetic moment significantly higher for Mn:bcc-In_2O_3. Surprisingly, X-ray magnetic circular dichroism (XMCD), as an element-specific measure of magnetic properties, reveals no essential role of Mn dopants as carriers of the magnetic moment in ferromagnetic samples. Based on recent theoretical considerations,[28] we propose that Mn dopant ions participate in charge transfer to the local density of states associated with interfacial structural defects, leading to Stoner splitting of the defect band states. The magnetization measurements of samples having different doping concentrations indicate that the long-range ordering mechanism changes from charge-transfer-based ferromagnetism at low doping concentrations to double exchange at doping levels approaching the percolation limit. The results of this work provide new experimental evidence for charge-transfer ferromagnetism in DMSOs and demonstrate the ability to control their magnetic properties by controlling the crystal structure of the host lattice, as well as the oxidation state of the dopant ions. The demonstrated assortment of tunable parameters enables the elucidation of the mechanism of magnetic interactions and, more broadly, the origin and manipulation of the complex functionalities in solid state.

EXPERIMENTAL SECTION

Chemicals. All reagents and solvents were used as received from the supplier with no further purification. Indium acetylacetonate ($In(acac)_3$, 98%), manganese chloride ($MnCl_2$, 97%), and manganese acetylacetonate ($Mn(acac)_2$) were purchased from STREM Chemicals. Manganese(III) acetylacetonate ($Mn(acac)_3$) was purchased from Alfa Aesar. Oleylamine (70%) and trioctylphosphine oxide (TOPO, 90%) were purchased from Sigma-Aldrich. Solvents include toluene (99.98%, EMD Chemicals), hexanes (99.9%, Fischer Scientific), and absolute ethanol.

Synthesis and Processing of Mn-Doped In_2O_3 Nanocrystals. The synthetic and processing methods utilized have been reported previously.[23,29] In a 100 mL three-neck round-bottom flask, 4 mmol of $In(acac)_3$ and different amounts (2 to 20 mol %) of manganese precursors were combined with 48 mmol of oleylamine. The content was degassed under an argon atmosphere and subsequently heated up to 250 °C, after which the reaction mixture was refluxed with constant stirring for a minimum of 1 h. Once the desired reaction time had been reached, the reaction mixture was cooled to room temperature. The resulting product was a viscous suspension of Mn:In_2O_3 NCs, which were precipitated through the addition of ethanol followed by centrifugation at 3000 rpm for 5 min. The process of washing NCs with ethanol followed by centrifugation was repeated three times. The NCs were then combined with an approximately equivalent volume of TOPO and heated with stirring at 90 °C for 1 h, after which the NCs were once again precipitated with ethanol and centrifuged. The TOPO treatment was completed a total of three times, ensuring that NC surfaces are free of surface-bound dopant ions, and increasing the solubility of the NCs in nonpolar organic solvents.[29] Treated NCs were suspended in hexane or toluene for analysis and measurements. All samples were handled in an identical fashion and kept under conditions free of contamination by magnetic materials and tools.

For magnetization measurements of nanocrystalline films (see below), colloidal NCs were spin-coated on sapphire substrates previously sonicated in aqua regia, followed by mild annealing at 300 °C for 1 min. The spin coating process was repeated multiple times until the mass of the nanocrystalline film reached at least 1 mg. Special precaution should be exercised when preparing and handling aqua regia. The aqua regia mixture was prepared by adding concentrated nitric to hydrochloric acid in a 1:3 (v/v) ratio in a Pyrex glass container. The preparation and subsequent substrate

treatment must be performed in an efficient, properly shielded fume hood, using personal protection clothing and face shield. The resulting mixture is a fuming yellow-to-orange solution which was used immediately after preparation.

Characterization and Measurements. Transmission electron microscopy (TEM) and energy dispersive X-ray spectroscopy (EDX) measurements were collected with a JEOL-2010F microscope operating at 200 kV. Samples were prepared using standard copper grids with lacey Formvar/carbon support films purchased from Ted Pella Inc. The average nanocrystal sizes and size distributions were determined based on the measurements of at least 150 NCs using Microstructure Measurement software. Powder X-ray diffraction (XRD) patterns were collected using an INEL diffractometer with a position-sensitive detector and monochromatic Cu Kα radiation (λ = 1.5418 Å). The synthesized and processed samples were dried, and the obtained powder was crushed and loaded onto an aluminum holder. For nanocrystalline films the substrates were attached directly onto the sample holder. The XRD patterns were collected for up to 10 h to obtain a high signal-to-noise ratio, particularly for nanocrystalline films.

The optical absorption spectra of Mn:In_2O_3 NCs were collected with a Varian Cary 5000 UV−vis−NIR spectrophotometer. The spectra were collected using 1 cm path-length quartz cuvettes for colloidal NCs and strain-free quartz substrates for low-temperature measurements. Magnetic circular dichroism (MCD) spectroscopy measurements were performed in a Faraday configuration with a Jasco J-815 spectropolarimeter. The NC samples deposited on strain-free quartz substrates were mounted in a variable magnetic field (0−8 T) superconducting magneto-optical cryostat (SM4000-8, Oxford Instruments) with a variable temperature insert (1.5−300 K). X-ray absorption spectroscopy (XAS) measurements were performed at the Canadian Light Source (CLS). Manganese K-edge X-ray absorption near-edge structure (XANES) and extended X-ray absorption fine structure (EXAFS) spectra were collected at the Hard X-ray MicroAnalysis (HXMA) beamline (06ID-1). Mn $L_{2,3}$-edge X-ray absorption and magnetic circular dichroism measurements were performed using scanning transmission X-ray microscopy (STXM) at the Soft X-ray Spectromicroscopy (SM) beamline (10ID-1). For these measurements a ferromagnetic sample was transferred from the nanocrystalline film on the silicon nitride window by dry pressing and then mounted on a ring magnet with a magnetic field strength of ~0.15 T (near ferromagnetic saturation). The magnet along with the silicon nitride window was placed on a custom-made sample holder. The image was collected at each energy point for both left and right circularly polarized light, and an image stack was generated. The spectral analysis from stacked images was done using Axis-2000 software. The experimental procedure and data analysis involved in these measurements have been detailed in our previous publication.[17]

Magnetization data were generated using a Physical Property Measurement System (PPMS, Quantum Design) in ACMS mode. The measurements were taken at temperatures ranging from 2 to 300 K and magnetic fields of 0−9 T. For magnetization measurements of free-standing NCs, the colloidal NC samples were precipitated with ethanol, dried, and loaded into sample capsules. For measurements of nanocrystalline films, the samples were prepared by spin-coating the colloidal NCs, as described above.

RESULTS AND DISCUSSION

Nanocrystal Structure and Composition. The ability to control the size of doped In_2O_3 NCs via reaction temperature and dopant precursor concentration allows for the manipulation of their crystal and electronic structures.[12,23] Although both Mn^{2+} and Mn^{3+} inhibit the NC growth, leading to stabilization of rh-In_2O_3 phase, this process appears to be more pronounced for Mn^{3+}. The TEM images of typical Mn:In_2O_3 NCs having similar doping concentrations but different average NC sizes are shown in Figure 1a−d. Figure 1a shows an overview TEM image of 9.5% Mn:In_2O_3 NCs synthesized using Mn^{2+} as a dopant precursor. The NCs have quasi-spherical

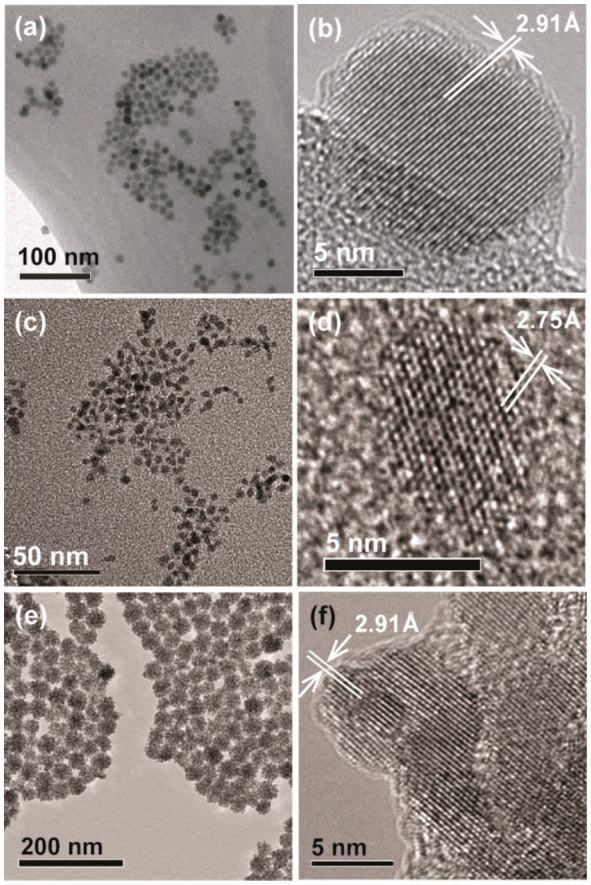

Figure 1. Overview (a,c,e) and high-resolution (b,d,f) TEM images of Mn:In_2O_3 NCs. (a,b) 9.5% Mn:bcc-In_2O_3 NCs. (c,d) 8.6% Mn:rh-In_2O_3 NCs. (e,f) 10.2% Mn:bcc-In_2O_3 nanoflowers. The measured lattice spacings indicated in high-resolution panels match the values for {222} (b and f) and {110} (d) planes of the corresponding phases.

shape and nearly uniform sizes with an average NC diameter of ca. 9.3 ± 1.3 nm. A lattice-resolved TEM image of a single NC from this sample is shown in Figure 1b. An average *d*-spacing of 2.91 Å corresponds to the {222} lattice plane of bcc-In_2O_3. On the other hand, 8.6% Mn:In_2O_3 NCs in Figure 1c, synthesized using Mn(III) as a dopant precursor, have an average size of ca. 5.5 ± 0.7 nm, while the lattice spacing of 2.75 Å, measured for an individual NC (Figure 1d), corresponds to the {110} plane of rh-In_2O_3. The high resolution images (Figure 1b and d) demonstrate that NCs are single crystalline, with no evidence of mixed phases. However, in contrast to bixbyite-type NCs, Mn:rh-In_2O_3 NCs obtained at high dopant precursor concentrations generally appear to have a more irregular shape, which is likely associated with the adsorption of dopant ions on NC surfaces.[23]

Controlling the surfaces by impurity adsorption from solution can also be used to build complex nanostructures via assembly of Mn:In_2O_3 NCs. Using $MnCl_2$ as a Mn dopant precursor resulted in hexagonally packed flower-like clusters of Mn:bcc-In_2O_3 NCs for a sufficiently high dopant precursor concentration (Figure 1e and Figure S1 in Supporting Information). These flower-like clusters have an average size of ca. 34 ± 5 nm and consist of aggregated Mn:bcc-In_2O_3 NCs. Closer inspection of the clusters reveals that lattice fringes corresponding to the {222} plane of bcc-In_2O_3 extend over a large area (Figure 1f), suggesting that NCs are joined by

dx.doi.org/10.1021/ja501888a | J. Am. Chem. Soc. 2014, 136, 7669−7679

oriented attachment. The formation of "nanoflowers" via oriented attachment has previously been observed for In_2O_3,[30] as well as indium–tin oxide (ITO) NCs.[31] This process has initially been explained[30] by "limited ligand protection" (LLP).[32] However, we have shown that the same structures can also be formed at a later stage of the synthesis.[31] Furthermore, while incomplete NC surface coverage by the coordinating ligands is necessary for NC contact formation, it does not explain the driving force for the oriented attachment. Control experiments involving different anions in the solution have indicated that flower-like cluster formation is correlated with the ionic strength of the reaction mixture. Increased ionic strength has been associated with anisotropic charging of the NC surfaces by Cl^- ions, which could lead to a local dipole moment formation,[33] inducing attractive van der Waals interactions and assembly of NCs.[34] Adsorption of Cl^- ions should also lead to a displacement of the coordinating organic ligands, contributing to the diminished protection of NC surfaces. These observations demonstrate in situ bottom-up formation of magnetically doped complex oxide nanostructures using colloidal NCs as building blocks.

Figure 2 shows XRD patterns of Mn-doped bcc-In_2O_3 (green trace) and rh-In_2O_3 (blue trace) NCs from Figure 1a and c,

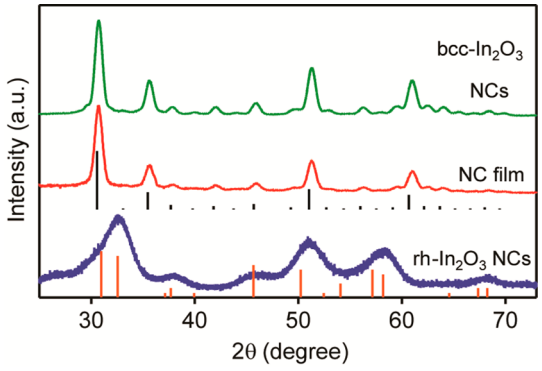

Figure 2. XRD patterns of 9.5% Mn:bcc-In_2O_3 NCs (green) and nanocrystalline film (red), and 8.6% Mn:rh-In_2O_3 NCs (blue). The XRD patterns of bulk bcc-In_2O_3 (JCPDS 06-0416) and rh-In_2O_3 (JCPDS 21-0406) are shown with black and orange lines, respectively.

respectively. These patterns also confirm the high crystallinity and phase purity of the samples, as evidenced from the comparison with the corresponding bulk patterns (vertical lines in Figure 2). The XRD peaks of Mn:rh-In_2O_3 NCs are significantly broadened owing to the small NC sizes. Importantly, typical nanocrystalline film, prepared from colloidal Mn:bcc-In_2O_3 NCs (red trace), displays a nearly identical pattern to that of colloidal NCs, with no evidence of Mn-related secondary phases.[35] The XRD peaks also appear to be shifted to slightly higher 2θ values relative to those for undoped bcc-In_2O_3, indicating a possible reduction in the unit cell size likely due to the incorporation of Mn^{3+}, which has a smaller ionic radius than In^{3+}.

Further insight into dopant incorporation can be obtained by STEM-EDX measurements. Figure 3a shows an EDX line scan of a single Mn:bcc-In_2O_3 NC. The line scan profiles of In (green trace) and Mn (red trace) are in very good agreement, indicating that Mn incorporation is largely homogeneous during NC growth.[36] The homogeneous dopant distribution is also demonstrated via EDX elemental mapping (Figure 3b–d). Similarly to line scan analysis of a single NC, the elemental

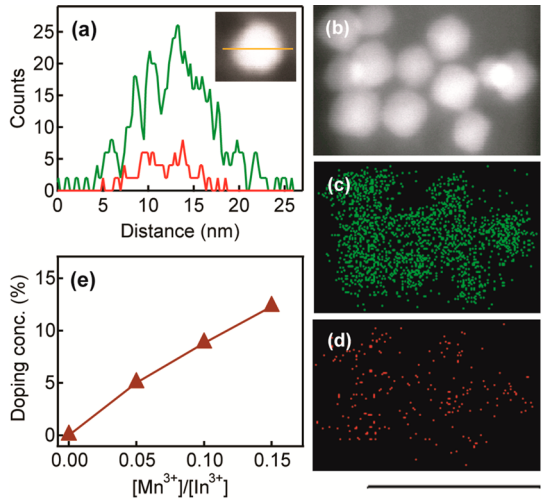

Figure 3. (a) Indium (green) and manganese (red) EDX elemental line scans for a typical Mn:bcc-In_2O_3 NC (shown in the inset). (b–d) STEM image (b) and the corresponding In (c) and Mn (d) EDX maps of an ensemble of 9.5% Mn:bcc-In_2O_3 NCs (scale bar, 60 nm). (e) Dependence of the Mn doping concentration on the initial dopant-to-host precursor concentration ratio.

maps of In and Mn (Figure 3c and d, respectively) in a NC ensemble (Figure 3b) are well-matched, with no evidence of Mn segregation. The Mn doping concentration steadily increases with increasing starting concentration of the dopant precursor in the reaction mixture, as shown in Figure 3e.

Manganese Dopant Oxidation States and Bond Distances. We studied the electronic structure of Mn dopant ions, including their oxidation states and the nature of the doping sites, using a variety of spectroscopic methods. Figure 4

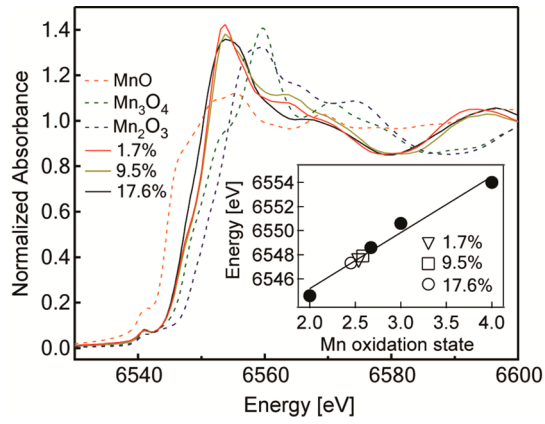

Figure 4. Normalized Mn K-edge XANES spectra of Mn:In_2O_3 NCs having different doping concentrations (solid lines) and typical reference compounds (dashed lines), as indicated in the graph. Inset: dependence of the reference spectra half-height energy on the Mn oxidation state (solid circles). The established dependence was used to infer the effective Mn oxidation state in Mn:In_2O_3 NC samples (open symbols).

shows Mn K-edge XANES spectra of Mn:In_2O_3 NCs prepared with different starting concentrations of the Mn(II) precursor (solid traces in Figure 4). These spectra are distinctly different from the XANES spectra of manganese oxides, used as typical references (dashed traces in Figure 4), corroborating the absence of these compounds as secondary phases in our

dx.doi.org/10.1021/ja501888a | J. Am. Chem. Soc. 2014, 136, 7669–7679

samples. The spectrum of the sample having a 17.9% doping concentration is slightly different from the spectra of the samples containing 1.7% and 9.5% dopants. The differences are mostly reflected through a more pronounced shoulder at ca. 6556 eV and the lack of features at ca. 6565 eV in 17.9% Mn:In_2O_3 NCs. Correlation with the XRD data reveals that XANES spectra of NCs having lower doping concentrations correspond to Mn in the bcc-In_2O_3 phase, while the spectrum of NCs having a higher doping concentration is associated with Mn in rh-In_2O_3. Importantly, the energy of the edge jump can be used to quantify the oxidation state of Mn in the samples of interest. This can be achieved through half-height energy or second derivative analysis of the spectral edge.[37] The inset in Figure 4 shows the half-height energy dependence on the Mn oxidation state. The half-height energies of reference compounds (black circles) are used for calibration, and the energies corresponding to samples having different doping concentrations are shown with the symbols designated in the graph. For both bcc- and rh-In_2O_3 NC phases, the effective oxidation state is between 2+ and 3+, indicating the presence of mixed oxidation states (Mn^{2+} and Mn^{3+}). Similar results were obtained for NCs synthesized using Mn(III) as a dopant precursor (Figure S2 and Table S1 in Supporting Information). Mn(III) is a moderately oxidizing agent,[24] which explains the possibility of the coexistence of Mn^{2+} and Mn^{3+}. The mechanism of this redox process, which likely occurs during NC growth, is beyond the scope of this work. The synthesis of In_2O_3 NCs is based on a complex mechanism in which hydrolysis catalyzed by oleylamine plays an important role, and we can speculate here that the oxidative synthetic conditions allow for the stabilization of Mn^{2+} and the formation of equilibrium between Mn^{2+} and Mn^{3+}. An important question in this context is the charge balance of the doped NC host lattice. While Mn^{3+} is isovalent with In^{3+}, incorporation of Mn^{2+} requires a charge compensation, which can be facilitated by an additional hole or suitable lattice defect formation. Given the n-type character and the propensity for oxygen vacancy formation in this TCO lattice, it is likely that incorporation of Mn^{2+} ions occurs concurrently with the formation of oxygen vacancies, which are also associated with magnetic properties of this material (*vide infra*).

Complementary information about the electronic structure of Mn dopants can be gained from the EXAFS spectroscopy (Figure 5 and Figure S3 in Supporting Information). Figure 5a shows baseline-corrected *k*-weighted Mn K-edge EXAFS spectra of the samples from Figure 4. The Fourier-filtered EXAFS spectra corresponding to the first coordination shell (Mn−O) are shown in Figure 5b (solid traces). These spectra were fit in the framework of the single-scattering theory (Figure 5b dashed traces). The structural parameters obtained from fitting of the Fourier-filtered EXAFS spectra using a linear combination of Mn−O distances characteristic for Mn^{2+} (in MnO) and Mn^{3+} in (Mn_2O_3) as the initial values[38] are summarized in Table 1. It should be noted that the agreement between Fourier-filtered spectra and the theoretical fits is significantly worse when Mn^{2+}−O and Mn^{3+}−O bond distances are used separately as the fitting parameters. We can now combine the results from Figures 4 and 5b to comprehensively describe the electronic structure of dopant ions by establishing a correlation between their oxidation states and structural parameters. Figure 5c and d plots the dependence of the fraction of Mn^{2+} (red symbols) and the corresponding Mn^{2+}−O bond distance (blue symbols) on the average doping

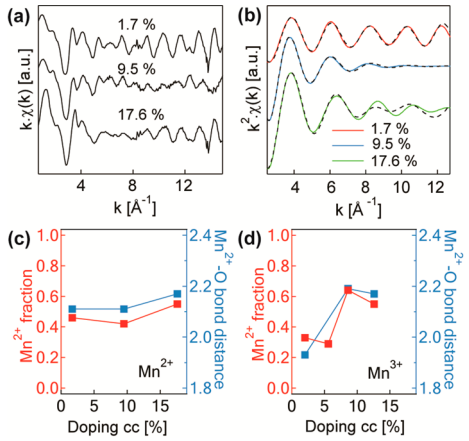

Figure 5. (a) *k*-weighted Mn K-edge EXAFS spectra of Mn:In_2O_3 NCs having different doping concentrations (shown in the graph). (b) Fourier-filtered EXAFS oscillations for the Mn−O (first) shell weighted by k^2. The functions were fitted assuming a combination of Mn^{2+} and Mn^{3+} oxidation states (dashed lines). (c,d) The dependence of Mn^{2+} fraction (left ordinate) and Mn^{2+}−O bond distance (right ordinate) on the doping concentration for the samples synthesized with Mn^{2+} (c) and Mn^{3+} (d) precursors.

concentration for the samples synthesized with Mn(II) and Mn(III) precursors, respectively. In both Figure 5c and d, the Mn^{2+} fraction is well correlated with the Mn^{2+}−O bond distance, and the two parameters increase with increasing doping concentration. Considering the similar ionic radii of Mn^{2+} and In^{3+} (0.83 and 0.80 Å, respectively) we expect that Mn^{2+}−O and In−O bond distances should be very similar. According to the literature reports,[39] an average In−O bond distance in both bixbyite and rhombohedral In_2O_3 lattices is 2.17−2.18 Å, which indeed agrees very well with the obtained Mn^{2+}−O distances at higher doping concentrations. For samples containing a lower Mn content in Figure 5d, Mn^{3+} with an ionic radius of 0.65 Å is the dominant species, leading to a general decrease in Mn−O bond distances, due to shrinking of the host lattice. These results indicate the important interdependence of the electronic structure of Mn dopant ions, host lattice crystal structure, and the lattice parameters on the choice and concentration of the dopant ion precursors, which can be used to manipulate the magnetic properties of these materials (*vide infra*).

Electronic Structure and Magnetic Circular Dichroism Spectroscopy of Mn Dopant Ions. Spectroscopic and magnetic properties of Mn:In_2O_3 NCs in colloidal form were studied by MCD spectroscopy, which is a very powerful technique for the molecular-level investigation of the electronic structure and magnetic interactions of transition metal centers. MCD measures magnetically induced chirality, or the difference in the absorption of left and right circularly polarized light between Zeeman-split ground and excited states. As such, MCD is directly related to ligand field electronic absorption spectroscopy.

Figure 6 shows absorption (top) and MCD (bottom) spectra of Mn-doped bcc-In_2O_3 (Figure 6a) and rh-In_2O_3 NCs (Figure 6b). The free Mn^{2+} ion has a $3d^5$ electronic configuration with a half-filled 3d shell, resulting in the ^6S ground state. All transitions from this ground state to the existing quartet or doublet excited states are spin-forbidden. Although Mn^{2+} transitions can gain some intensity in a crystal field, they are generally characterized by very small extinction coefficients

dx.doi.org/10.1021/ja501888a | J. Am. Chem. Soc. 2014, 136, 7669−7679

Table 1. Structural Parameters Obtained through the EXAFS Analysis of Mn:In_2O_3 NCs

dopant precursor	doping concentration [%]	distance (Mn^{2+}–O) [Å]	distance (Mn^{3+}–O) [Å]	σ^2 (Mn^{2+}) [$Å^2$][a]	σ^2 (Mn^{3+}) [$Å^2$][a]	ρ [%][b]
Mn(II)	1.7	2.11	1.94	0.005	0.002	0.34
	9.5	2.11	1.96	0.034	0.018	0.54
	17.6	2.17	1.89	0.020	0.009	0.46
Mn(III)	2.0	1.93	1.73	0.011	0.034	0.92
	8.6	2.19	1.87	0.008	0.021	0.10
	12.7	2.17	2.07	0.005	0.005	0.49

[a]Debye–Waller factor. [b]Weighted residual factor.

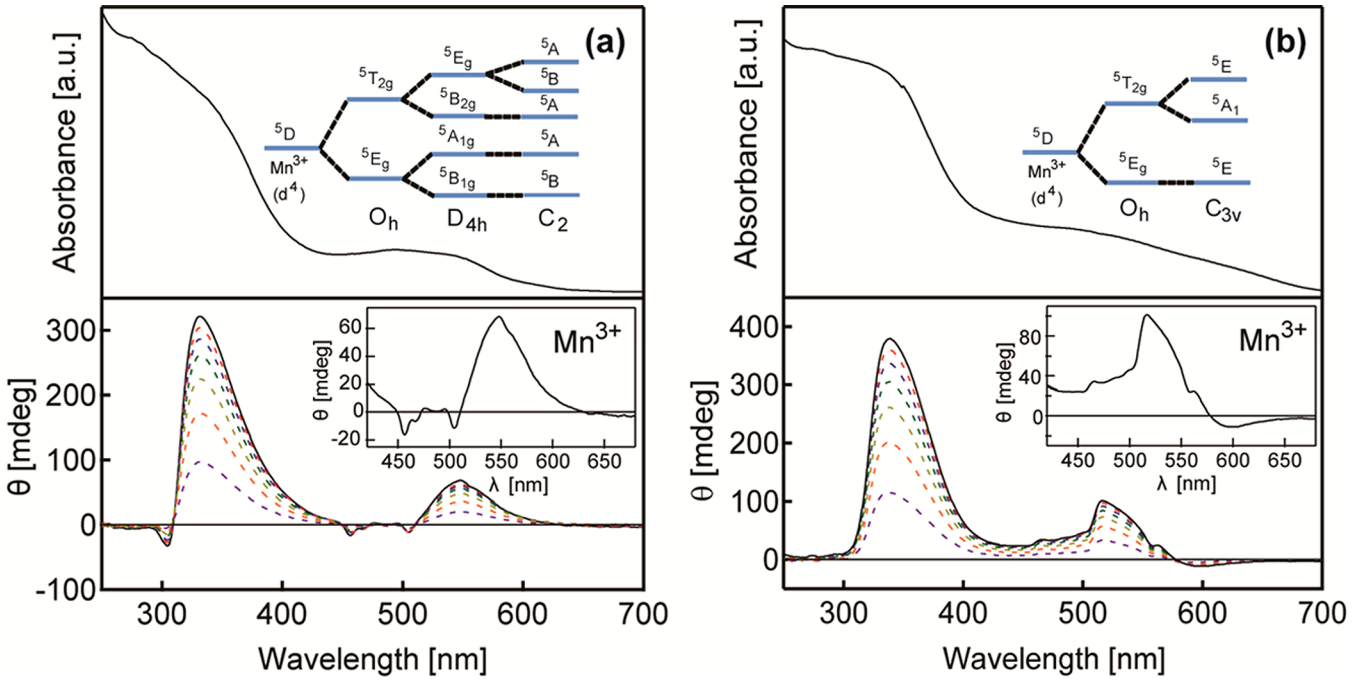

Figure 6. 5 K ligand field electronic absorption (top) and MCD (bottom) spectra of typical (a) Mn:bcc-In_2O_3 and (b) Mn:rh-In_2O_3 NCs. Insets: (top panels) splitting pattern of Mn^{3+} electronic states in relevant point group symmetries; (bottom panels) magnified high resolution spectra of Mn^{3+} ligand field transitions. See text for details.

(10^{-2}–10^{-1} cm^{-1} M^{-1}). On the other hand, high-spin octahedral Mn^{3+} ions (d^4 configuration) exhibit robust spin-allowed transitions, associated with splitting of the free ion ^5D ground state into $^5T_{2g}$ and ^5E_g terms. This splitting results in a strong $^5E_g \rightarrow {}^5T_{2g}$ spin-allowed transition, which usually appears in the visible spectral region at ca. 20,000 cm^{-1}.[24] In other nonoctahedral six-coordinate complexes, $^5T_{2g}$ and ^5E_g terms split further into A and B terms. Furthermore, as a d^4 system, Mn^{3+} is subject to Jahn–Teller distortion,[40] which leads to additional splitting of the ^5E ground state, resulting in low-energy absorption features. In the trigonal field characteristic for substitutionally doped Mn^{3+} in a corundum crystal structure (trigonally distorted octahedral coordination, C_{3v} point group), the ^5E ground state is degenerate, while the $^5T_2$ term splits into two components, $^5A_1$ and ^5E.[41]

Using these considerations we can first assign the observed features in Figure 6b. The pronounced asymmetric band at ca. 520 nm in the MCD spectrum originates mostly from the $^5E \rightarrow {}^5A_1$ transition, and a weaker structured band centered at 485 nm from the $^5E \rightarrow {}^5E$ transition of Mn^{3+} in rh-In_2O_3 (inset in Figure 6b). These features appear only as shoulders in the absorption spectrum (Figure 6b, top) owing to the higher sensitivity of MCD spectroscopy to metal-centered ligand field transitions. The most dominant feature in the absorption spectrum is a broad shoulder centered at ca. 340 nm, which corresponds to the NC band gap absorption. Importantly, this band gap transition is also observed in the MCD spectrum as a well-defined band. A lower energy shoulder in the absorption spectrum at ca. 630 nm, corresponding to a weak MCD band having a negative sign, is likely associated with low-lying charge transfer transition, and possibly some contribution from the Jahn–Teller distortion of the ground state.[41−43]

The situation is more complicated for Mn^{3+} in bcc-In_2O_3, which possesses two possible substitutional sites in a unit cell, *b* (8) and *d* (24) sites, having S_6 (or C_{3i}) and C_2 point group symmetry, respectively. The *b* sites can be described as trigonally compressed, and the *d* sites, as highly distorted octahedra. Computational studies have suggested that a dopant cation smaller than the host lattice cation preferentially occupies a *d* site, and a dopant cation larger than the host cation the *b* site.[44] Comparison between MCD spectra of Cr^{3+} (having octahedrally coordinated radius of 0.62 Å) in bcc- and rh-In_2O_3 is shown to be consistent with Cr^{3+} occupying the lower symmetry *d* site in bcc-In_2O_3.[14] Given its ionic radius of 0.65 Å, Mn^{3+} is also expected to reside on a *d* site.

The visible absorption spectrum of Mn:bcc-In_2O_3 (Figure 6a, top) consists of two broad overlapping shoulders, which coincide with a relatively broad transition centered at ca. 550

dx.doi.org/10.1021/ja501888a | J. Am. Chem. Soc. 2014, 136, 7669–7679

nm and a set of narrow negative and positive bands between ca. 450 and 500 nm in the MCD spectrum (Figure 6a, bottom). Richly structured spectra of Mn^{3+} in bcc-In_2O_3, particularly in the 450−500 nm range, suggests a lower symmetry site for Mn^{3+} in bcc-In_2O_3 relative to rh-In_2O_3 NCs. This observation is consistent with preferential *d* site occupancy by Mn^{3+} dopants. In analogy to Mn^{3+} in rh-In_2O_3 NCs, the spectral features in Figure 6a can be predominantly associated with components of $^5T_{2g}$, resulting from the reduction in symmetry. More insight into these features can be obtained by considering the splitting pattern of d^4 ion energy states in a rhombic (C_{2h}) environment,[24] which is structurally similar to the *d* site in bcc-In_2O_3 (top inset in Figure 6a). The low energy broad band peaking at ca. 550 nm is associated with the transition between the ground state and the lowest-lying $^5T_{2g}$ component ($^5B \rightarrow {}^5A$, originating from $^5B_{1g} \rightarrow {}^5B_{2g}$ in the ideal tetragonal environment), while the higher energy narrow bands at ca. 500 and 450 nm are assigned to the transitions from the ground state to ^5B and ^5A, respectively, derived from ^5E_g in D_{4h} symmetry. It is also possible that the low energy side of a broad asymmetric band with a maximum at ca. 550 nm ($^5B \rightarrow {}^5A$) originates from ground state splitting due to Jahn−Teller distortion.[42] Similarly to the MCD spectrum of Mn:rh-In_2O_3 NCs, band gap transition is observed for the Mn:bcc-In_2O_3 NCs at ca. 330 nm. In contrast to the Mn^{3+} dopant, Mn^{2+} is expected to substitute for In^{3+} sitting in the more symmetric *b* site, based on its ionic radius. This analysis indicates the possibility of controlling the distribution of dopant ions between two different substitutional sites and their electronic structure, using chemical means.

Additional insight into the electronic structure and magnetic exchange interactions of Mn dopants in In_2O_3 NCs can be inferred from the magnetic field dependence of MCD spectra. The MCD spectra were recorded in different fields (1−7 T), shown with dashed lines in Figure 6. The magnetic field dependence of the intensity of MCD transitions at different wavelengths are plotted in Figure 7 for Mn:bcc-In_2O_3 (Figure 7a) and Mn:rh-In_2O_3 NCs (Figure 7b). In both samples, the magnetization properties of Mn^{3+} can be represented by the field dependence of the MCD intensity at the maximum of the band corresponding to the transition from the ground state to the lowest lying component of $^5T_{2g}$ at 548 and 516 nm for Mn:bcc-In_2O_3 and Mn:rh-In_2O_3 NCs, respectively. The MCD intensities saturate at high magnetic fields and low temperatures. These data are readily fit to the spin-only Brillouin function describing the saturation magnetization (M_s) behavior:

$$M_s = \frac{1}{2}Ng\mu_B\left[(2S+1)\coth\left((2S+1)\left(\frac{g\mu_B H}{2k_B T}\right)\right) - \coth\left(\frac{g\mu_B H}{2k_B T}\right)\right] \quad (1)$$

where S is the spin state, g is the Lande *g*-factor, H is the magnetic field strength, T is the temperature, and N, μ_B, and k are the number density of dopant centers, the Bohr magneton, and the Boltzmann constant, respectively. According to the literature,[45] for Mn ions in rhombohedral and cubic oxides, $g \approx 1.98-2.00$. The best fits to the experimental data points are obtained by considering only the spin state of Mn^{3+} substituting for In^{3+} (for the high-spin d^4 system $S = 2$). This result is consistent with the above discussion about the electronic structure of Mn^{2+}, which does not contribute to the MCD spectra. Fitting with the spin-only Brillouin function is a result of the absence of the orbital angular momentum in the ^5E_g ground state of Mn^{3+}. Importantly, the band gap transitions measured at 332 and 340 nm in Figure 7a and b, respectively, are also dependent on the applied magnetic field strength. The MCD intensities of the band gap transitions mostly follow the behavior observed for Mn^{3+} transitions. The presence of the band gap transition in MCD spectra and its magnetic field dependence suggest that dopant ions undergo exchange coupling with the band structure of the NC host lattice, via sp−d exchange interactions.[9,10]

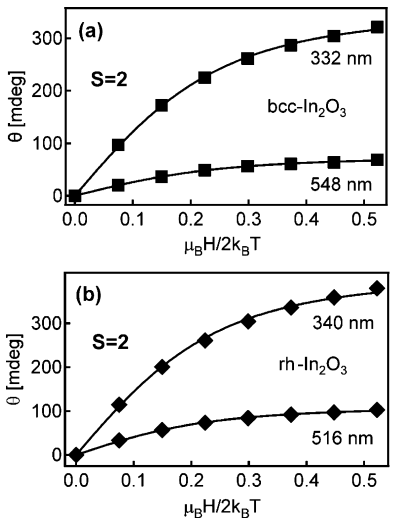

Figure 7. Magnetic field dependence of the intensity of MCD spectra of (a) Mn:bcc-In_2O_3 and (b) Mn:rh-In_2O_3 NCs at selected wavelengths, as indicated in the graphs. The experimental data (solid squares) were fit with the Brillouin function (eq 1) for the spin quantum number $S = 2$.

Magnetization Measurements of Nanocrystalline Mn-Doped In_2O_3. The results of MCD spectroscopy were correlated with those of the magnetic susceptibility measurements (Figure 8). Figure 8a (open circles) shows saturation magnetization data for free-standing 9.5% Mn:In_2O_3 NCs collected at 2 K in the field range 0−9 T. The magnetization saturates at high magnetic field and low temperature, indicating paramagnetic behavior. These data are compared with saturation magnetization curves for Mn^{2+} and Mn^{3+} calculated using the Brillouin function (dashed lines in Figure 8a). Neither Mn^{2+} nor Mn^{3+} Brillouin functions alone match the experimental data. On the other hand, a linear combination of Brillouin functions for both species ($M_s = xM_s(Mn^{2+}) + yM_s(Mn^{3+})$, where $x + y = 1$) results in a very good fit to the experimental data. This analysis reveals that the best fit is obtained for ca. 60% of Mn^{3+} and 40% of Mn^{2+}, which is in excellent agreement with X-ray absorption spectroscopy data for 9.5% Mn:In_2O_3 NCs (Figure 5). Similar observations were made for Mn:In_2O_3 NCs synthesized with the Mn(III) precursor.

Colloidal paramagnetic DMSO NCs have been used as nanoscale building blocks for the preparation of films on nonmagnetic substrates, which exhibit long-range ferromagnetic ordering of dopant ions.[9,10,16−18] The long-range magnetic ordering has been related to the formation of interfacial grain boundaries, which are proposed to contain oxygen vacancies as

dx.doi.org/10.1021/ja501888a | J. Am. Chem. Soc. 2014, 136, 7669−7679

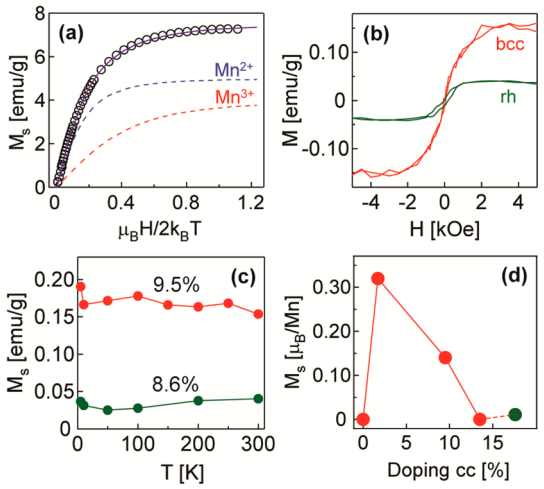

Figure 8. (a) 2 K saturation magnetization of free-standing 9.5% Mn:bcc-In_2O_3 NCs (open circles). The best fit is obtained using the Brillouin function for 60% Mn^{3+} (red line) and 40% Mn^{2+} (blue line). (b) 300 K magnetization hysteresis loops for 9.5% Mn:bcc-In_2O_3 (red) and 8.6% Mn:rh-In_2O_3 nanocrystalline films. (c) Temperature dependence of the saturation magnetization for the nanocrystalline films in (b). (d) Concentration dependence of the saturation magnetization of Mn:In_2O_3 nanocrystalline films. Red circles indicate bcc-In_2O_3 and green circles rh-In_2O_3 phase.

key structural defects.[9,18] Figure 8b compares the hysteresis loops for Mn:In_2O_3 nanocrystalline films prepared from NCs synthesized using Mn^{2+} (red trace) and Mn^{3+} (green trace) as dopant precursors. Although these samples have similar doping concentrations (9.5% for NC synthesized using Mn^{2+}, and 8.6% for NCs synthesized using Mn^{3+}) the saturation magnetic moments are significantly different. Nanocrystalline films consisting of 9.5% Mn:In_2O_3 NCs have a nearly 4 times larger saturation magnetic moment. However, both samples remain ferromagnetic at least up to room temperature, as evident from the temperature dependence of the saturation magnetization in Figure 8c. Magnetization hysteresis curves collected at different temperatures for 9.5% Mn:In_2O_3 nanocrystalline films are shown in Figure S4 (Supporting Information). The doping concentration dependence of the saturation magnetic moment is shown in Figure 8d. The measured magnetization initially rapidly increases, followed by a gradual decrease with increasing doping concentration. The highest magnetic moment (~0.32 μ_B/Mn) was measured for a ca. 2% Mn doping concentration. The residual zero-field magnetization at 300 K for this sample is ca. 0.02 μ_B/Mn. At doping concentrations approaching 20% (green circle), the magnetic moment increases again, which is accompanied by the change in the nanocrystal phase from bcc- to rh-In_2O_3.

Mechanism of Ferromagnetic Ordering. How can the results of the magnetization measurements be rationalized in the context of the electronic structure of this complex system? This discussion should start with the well-established conclusion that traditional descriptions of exchange interactions (i.e., double exchange, superexchange, and RKKY) cannot account for room-temperature ferromagnetic ordering of dilute, randomly distributed magnetic dopants in oxide matrices.[28,46] Furthermore, the presence of extended structural defects, such as grain boundaries or surface states in different nanostructured materials, appears to be necessary for dilute ferromagnetism.[47] These observations indicate that long-range ordering might only indirectly be related to the presence of paramagnetic dopant ions. An important and unique aspect of the system described in this work is that it unambiguously contains mixed oxidation states of dopant ions. A recent article has proposed that this feature could be associated with spin splitting of the defect band induced by the charge transfer involving dopant ions.[28] According to this model, an electron is transferred from the reduced form of the dopant ion (Mn^{2+} in this case) to the local defect density of states, raising the Fermi level to a peak in the local density of states and causing the spin splitting of the defect band (Figure 9). This process can, in principle, also

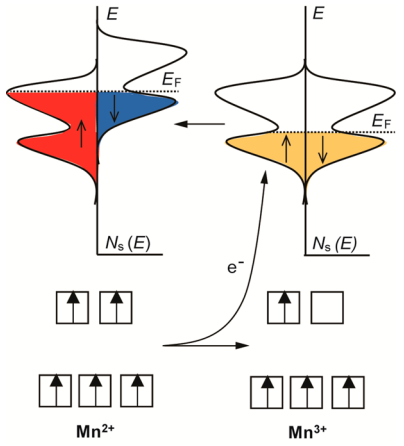

Figure 9. Schematic representation of the proposed charge-transfer ferromagnetism in nanocrystalline DMSOs containing mixed-valence transition metal dopants. This mechanism involves electron transfer from Mn^{2+} to the local density of states ($N_s(E)$) associated with the interfacial structural defects, raising the Fermi level to a peak in $N_s(E)$ and causing Stoner splitting of the defect band (indicated with red and blue colors).

occur in the opposite direction (i.e., a dopant ion can accept an electron from the defect band states, lowering the Fermi level). If the energy gain of the spin splitting is larger than the energy required for the charge transfer, the percolated defect states will form a net magnetic moment. The role of transition metal ions in this model is not to provide a source for a magnetic moment, but to facilitate the charge transfer processes. The presence of mixed-valence dopant cations is, therefore, an essential property of this charge-transfer ferromagnetism.

In this work the fraction of Mn^{2+}/Mn^{3+} is comparable in all samples, indicating a similar degree of charge transfer in the framework of the charge-transfer mechanism of ferromagnetic ordering. It is also important to compare the hysteresis loops in Figure 8b. The saturation magnetization is much smaller for the 8.6% Mn:In_2O_3 nanocrystalline film, although both samples contain similar concentrations of dopants and a comparable ratio of $[Mn^{2+}]/[Mn^{3+}]$. However, the constituent NCs containing 8.6% Mn dopants have rh-In_2O_3 structure. We have previously shown that smaller rh-In_2O_3 NCs generally exhibit a wider band gap relative to bcc-In_2O_3 NCs, which was also confirmed for these particular samples by absorption spectroscopy.[12,31] This phenomenon may also lead to an increase in the charge transfer energy between dopant ions and the defect-related band in rh-In_2O_3 NCs, thereby reducing the magnitude of the band spin splitting and the resulting magnetization. In addition to the mixed dopant ion oxidation states, charge-transfer-based ferromagnetism assumes other

dx.doi.org/10.1021/ja501888a | J. Am. Chem. Soc. 2014, 136, 7669−7679

important hypotheses, which can be qualitatively or quantitatively tested.

(1) Most of the magnetization comes from the defect-rich region (i.e., in the vicinity of the grain boundaries), which enables more energetically favorable charge transfer between dopant ions and the local defect density of states. This condition is fulfilled in the case of the high surface area nanocrystalline films assembled from colloidal NCs.
(2) The maximum net magnetic moment is 1 Bohr magneton per transition metal dopant, since each dopant ion can donate/accept at most one electron. In this work, the largest measured magnetic moment suggests that up to ca. 30% of dopant ions effectively participate in charge-transfer ferromagnetism.
(3) The spin state of a dopant ion is not relevant for the charge transfer process and, as such, does not influence the measured magnetic moment.

This last point is the most intriguing and fundamentally inherent to this mechanism. Testing of this hypothesis requires investigation of ferromagnetism at the molecular level. X-ray magnetic circular dichroism is a sensitive element-specific probe of magnetization and is a powerful tool for directly understanding the origin and mechanism of magnetic ordering.[48] Here, we performed XMCD measurements by STXM, allowing for magnetization-induced spectroscopic imaging of the Mn dopants with high spatial resolution. Figure 10 (top) shows Mn

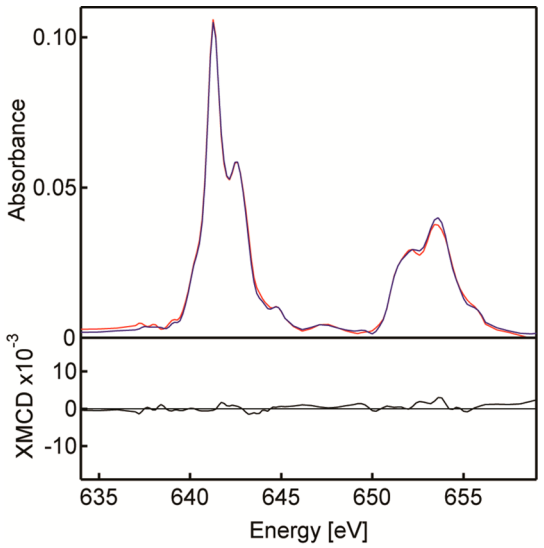

Figure 10. (Top) Manganese $L_{2,3}$-edge X-ray absorption spectra of ferromagnetic 9.5% Mn:bcc-In_2O_3 nanocrystalline film collected by STXM using left (blue line) and right (red line) circularly polarized photons. The resulting XMCD spectrum (bottom) shows no distinct features.

$L_{2,3}$-edge absorption spectra for the ferromagnetic 9.5% Mn:bcc-In_2O_3 nanocrystalline film from Figure 8b, collected using left circularly polarized (LCP) and right circularly polarized (RCP) photons. An STXM image of the sample corresponding to the spectra in Figure 10 is shown in Figure S5 (Supporting Information). The spectra are nearly identical, resulting in negligible XMCD intensity (bottom part in Figure 10). This result is in clear contrast with the results of XMCD imaging of diluted magnetic nanostructures, in which ferromagnetism arises from long-range magnetic exchange interactions involving dopant ions.[17,49,50] For instance, we have shown that Mn dopants in GaN nanowires exhibit a distinct L-edge XMCD spectrum, as a consequence of mediated magnetic exchange interactions.[49] The calculated Mn L-edge XMCD spectrum involving Mn exchange interactions delocalized over the In_2O_3 lattice (i.e., itinerant electron or defect-mediated ferromagnetism) is shown in Figure S6 (Supporting Information). These results unambiguously confirm that Mn dopants do not directly participate in exchange interactions in nanocrystalline Mn:bcc-In_2O_3 ferromagnetic films. Furthermore, ferromagnetism associated with secondary phases would also be based on Mn exchange interactions, and these results rule out that dopant segregation could be the origin of the observed ferromagnetism.

The maximum saturation magnetization in this work is obtained at relatively small doping concentrations. As the doping concentration increases beyond ca. 2%, the net magnetic moment decreases, which is likely associated with a statistical increase in the concentration of antiferromagnetically coupled pairs of dopant ions. However, at doping concentrations approaching 20% the net magnetic moment increases again. At these doping levels, the concentration of Mn dopants reaches the percolation limit, allowing for an extended coupling between next-to-nearest neighbor cations through a nonmagnetic anion. It is likely that this coupling is dominated by double exchange, owing to the different oxidation states of dopant ions present in comparable concentrations.

It is also instructive to correlate these results to other reports in the literature. It has been demonstrated that DMSOs containing dopant ions in a single oxidation state exhibit intrinsic defect-induced ferromagnetism involving exchange interactions of transition metal dopants.[17,20,51] Furthermore, the role of charge carriers in mediating magnetic ordering in DMSO NCs has also been demonstrated.[6] In light of the current results, it is plausible that different mechanisms of ferromagnetic ordering in nonmagnetic oxides are possible and, in some cases, could even coexist in the same material. These mechanisms are determined by the electronic structure of the NC host lattice and dopant ions, as well as the NC interfacial defect formation. Finally, it is warranted to briefly discuss the possible implementation of the mechanism reported in this work. The concept of charge-transfer ferromagnetism suggests that magnetic ordering in semiconductor oxides could in principle be achieved using different sources of charge carriers, including adsorbed molecular species or even externally injected carriers. These possibilities suggest various avenues of future experimental and theoretical research and provide a rich palette of possible applications of this class of materials. For instance, one can envision the possibility of controlling ferromagnetism using chemical, electrochemical, electrical, or optical methods. However, the application of these systems as spin polarizers and injectors will ultimately depend on the ability to precisely control the concentration and properties of native defects in reduced dimensions, necessitating further systematic research of the defect formation in nanostructures.

■ CONCLUSIONS

In summary, using colloidal Mn:In_2O_3 NCs as a case study, we provided experimental evidence for charge-transfer ferromagnetism, as an emerging form of ferromagnetic interactions in nanocrystalline TCOs. The uniqueness of this system relative to many other DMSOs reported in the literature is the ability to

control the host lattice structure based on the NC size and growth kinetics, as well as the existence of substitutional Mn dopant ions in mixed oxidation states (Mn^{2+} and Mn^{3+}). The existence of dopant ions in two different oxidation states allows for charge transfer between dopant ions and the local density of states associated with extended structural defects, which leads to Stoner-like splitting of the defect band and the formation of a net magnetic moment. Change of the host lattice phase from bcc-In_2O_3 to rh-In_2O_3 increases the energy cost of the charge transfer, reducing the magnitude of the measured magnetic moment. The essential feature of this mechanism is that dopant ions do not participate in magnetic exchange interactions and, therefore, do not have a role as a source for the magnetic moment. This feature was directly confirmed using XMCD spectromicroscopy, as a direct element-specific method for measuring the origin of ferromagnetism. Furthermore, as the doping concentration approaches the percolation limit, this mechanism begins to compete with "traditional" mechanisms of ferromagnetism, such as double exchange. Although the theoretical description of charge-transfer ferromagnetism requires additional refinement, the basic contours of this new mechanism are beginning to emerge, supported by the experimental evidence in this work. Given the range of convincing results on DMSO NCs in the literature, it is likely that multiple different mechanisms of long-range magnetic ordering are possible in these materials, depending on the electronic structure and concentration of dopant ions, host lattice, and structural defects. While these interdependencies introduce notable complexity, they also provide a significant opportunity for designing and manipulating the multifunctional properties involving magnetic interactions at the nanoscale.

■ ASSOCIATED CONTENT

Supporting Information

TEM images of Mn:bcc-In_2O_3 nanoflowers, XANES and EXAFS spectra and analysis of Mn:In_2O_3 NCs synthesized with $Mn(acac)_3$ dopant precursor, additional magnetization hysteresis curves, STXM image of the ferromagnetic Mn:In_2O_3 nanocrystalline film corresponding to XMCD data, calculated XMCD spectra. This material is available free of charge via the Internet at http://pubs.acs.org.

■ AUTHOR INFORMATION

Corresponding Author

pavler@uwaterloo.ca

Author Contributions

‡S.S.F. and T.S. contributed equally.

Notes

The authors declare no competing financial interest.

■ ACKNOWLEDGMENTS

This work was supported by the Natural Sciences and Engineering Research Council of Canada through the Discovery and RTI grants, Canada Foundation for Innovation (CFI), and Ontario Ministry of Research and Innovation (Early Researcher Award to P.V.R.). P.V.R. is Canada Research Chair in Spectroscopy of Nanoscale Materials. S.S.F. thanks Waterloo Institute for Nanotechnology (WIN) for a Graduate Research Fellowship. S.S.F. and M.H. acknowledge Canadian Light Source (CLS) for Graduate Travel Awards. X-ray spectroscopy experiments were performed at CLS, which is supported by the NSERC, NRC, CIHR, the Province of Saskatchewan, Western Economic Diversification Canada, and the University of Saskatchewan. We thank Drs. Ning Chen (06ID-1) and Jian Wang (10ID-1) for their assistance at respective beamlines.

■ REFERENCES

(1) (a) Lottermoser, T.; Lonkai, T.; Amann, U.; Hohlwein, D.; Ihringer, J.; Fiebig, M. *Nature* **2004**, *430*, 541−544. (b) Beaulac, R.; Schneider, L.; Archer, P. I.; Bacher, G.; Gamelin, D. R. *Science* **2009**, *325*, 973−976. (c) Buckley, B. B.; Fuchs, G. D.; Bassett, L. C.; Awschalom, D. D. *Science* **2010**, *330*, 1212−1215. (d) Ohno, H. *Science* **1998**, *281*, 951−956.

(2) Fert, A. *Angew. Chem., Int. Ed.* **2008**, *47*, 5956−5967.

(3) Furdyna, J. K. *J. Appl. Phys.* **1988**, *64*, R29−R64.

(4) Zutic, I.; Fabian, J.; Das Sarma, S. *Rev. Mod. Phys.* **2004**, *76*, 323−410.

(5) (a) Rangaraju, N.; Peters, J. A.; Wessels, B. W. *Phys. Rev. Lett.* **2010**, *105*, 117202. (b) Lee, J.; Oszwałdowski, R.; Gothgen, C.; Zutic, I. *Phys. Rev. B* **2012**, *85*, 045314.

(6) Ochsenbein, S. T.; Feng, Y.; Whitaker, K. M.; Badaeva, E.; Liu, W. K.; Li, X.; Gamelin, D. R. *Nat. Nanotechnol.* **2009**, *4*, 681−687.

(7) (a) Oszwałdowski, R.; Zutic, I.; Petukhov, A. G. *Phys. Rev. Lett.* **2011**, *106*, 177201. (b) Oszwałdowski, R.; Stano, P.; Petukhov, A. G.; Zutic, I. *Phys. Rev. B* **2012**, *86*, 201408(R).

(8) (a) Matsumoto, Y.; Murakami, M.; Shono, T.; Hasegawa, T.; Fukumura, T.; Kawasaki, M.; Ahmet, P.; Chikyow, T.; Koshihara, S.; Koinuma, H. *Science* **2001**, *291*, 854−856. (b) Ueda, K.; Tabata, H.; Kawai, T. *Appl. Phys. Lett.* **2001**, *79*, 988−990.

(9) Radovanovic, P. V.; Gamelin, D. R. *Phys. Rev. Lett.* **2003**, *91*, 157202.

(10) Schwartz, D. A.; Norberg, N. S.; Nguyen, Q. P.; Parker, J. M.; Gamelin, D. R. *J. Am. Chem. Soc.* **2003**, *125*, 13205−13218.

(11) (a) Hamberg, I.; Granqvist, C. G. *J. Appl. Phys.* **1986**, *60*, R123−R159. (b) Gurlo, A.; Kroll, P.; Riedel, R. *Chem.—Eur. J.* **2008**, *14*, 3306−3310. (c) Buonsanti, R.; Llordes, A.; Aloni, S.; Helms, B. A.; Milliron, D. J. *Nano Lett.* **2011**, *11*, 4706−4710. (d) Liu, W.; Xiu, F.; Sun, K.; Xie, Y.-H.; Wang, K. L.; Wang, Y.; Zou, J.; Yang, Z.; Liu, J. *J. Am. Chem. Soc.* **2010**, *132*, 2498−2499. (e) Farvid, S. S.; Wang, T.; Radovanovic, P. V. *J. Am. Chem. Soc.* **2011**, *133*, 6711−6719.

(12) Farvid, S. S.; Dave, N.; Radovanovic, P. V. *Chem. Mater.* **2010**, *22*, 9−11.

(13) Dietl, T. *Nat. Mater.* **2010**, *9*, 965−974.

(14) Farvid, S. S.; Ju, L.; Worden, M.; Radovanovic, P. V. *J. Phys. Chem. C* **2008**, *112*, 17755−17759.

(15) Singhal, A.; Achary, S. N.; Manjanna, J.; Jayakumar, O. D.; Kadam, R. M.; Tyagi, A. K. *J. Phys. Chem. C* **2009**, *113*, 3600−3606.

(16) Ronning, C.; Gao, P. X.; Ding, Y.; Wang, Z. L. *Appl. Phys. Lett.* **2004**, *84*, 783−785.

(17) Farvid, S. S.; Hegde, M.; Radovanovic, P. V. *Chem. Mater.* **2013**, *25*, 233−244.

(18) Archer, P. I.; Radovanovic, P. V.; Heald, S. M.; Gamelin, D. R. *J. Am. Chem. Soc.* **2005**, *127*, 14479−14487.

(19) Coey, J. M. D.; Venkatesan, M.; Fitzgerald, C. B. *Nat. Mater.* **2005**, *4*, 173−179.

(20) Kittilstved, K. R.; Liu, W. K.; Gamelin, D. R. *Nat. Mater.* **2006**, *5*, 291−297.

(21) (a) Coey, J. M. D.; Venkatesan, M.; Stamenov, P.; Fitzgerald, C. B.; Dorneles, L. S. *Phys. Rev. B* **2005**, *72*, 024450. (b) Sundaresan, A.; Bhargavi, R.; Rangarajan, N.; Siddesh, U.; Rao, C. N. R. *Phys. Rev. B* **2006**, *74*, 161306(R).

(22) Venkatesan, M.; Gunning, R. D.; Stamenov, P.; Coey, J. M. D. *J. Appl. Phys.* **2008**, *103*, 07D135.

(23) Farvid, S. S.; Dave, N.; Wang, T.; Radovanovic, P. V. *J. Phys. Chem. C* **2009**, *113*, 15928−15933.

(24) Lever, A. B. P. *Inorganic Electronic Spectroscopy*, 2nd ed.; Elsevier Science Publishers: Amsterdam, 1984.

(25) Karazhanov, S. Z.; Ravindran, P.; Vajeeston, P.; Ulyashin, A.; Finstad, T. G.; Fjellvåg, H. *Phys. Rev. B* **2007**, *76*, 075129.

(26) Berardan, D.; Guilmeau, E.; Pelloquin, D. *J. Magn. Magn. Mater.* **2008**, *320*, 983−989.
(27) Feng, Q.; Blythe, H. J.; Jiang, F.-X.; Xu, X.-H.; Heald, S. M.; Fox, A. M.; Gehring, G. A. *APL Mater.* **2013**, *1*, 022107.
(28) Coey, J. M. D.; Wongsaprom, K.; Alaria, J.; Venkatesan, M. *J. Phys. D* **2008**, *41*, 134012.
(29) Dave, N.; Pautler, B. G.; Farvid, S. S.; Radovanovic, P. V. *Nanotechnology* **2010**, *21*, 134023.
(30) Narayanaswamy, A.; Xu, H.; Pradhan, N.; Kim, M.; Peng, X. *J. Am. Chem. Soc.* **2006**, *128*, 10310−10319.
(31) Wang, T.; Radovanovic, P. V. *J. Phys. Chem. C* **2011**, *115*, 406−413.
(32) The LLP mechanism suggests the NCs spontaneously undergo oriented attachment in the early stage of growth when they are not well-developed and when there is diminished stabilization by organic ligands.
(33) Shim, M.; Guyot-Sionnest, P. *J. Chem. Phys.* **1999**, *111*, 6955−6964.
(34) Cho, K.-S.; Talapin, D. V.; Gaschler, W.; Murray, C. B. *J. Am. Chem. Soc.* **2005**, *127*, 7140−7147.
(35) These findings are in agreement with the previous reports involving the preparation of magnetic nanocrystalline films by spin coating of colloidal DMSO NCs (refs 9, 10, 14, and 17) which prevents the expulsion of dopant ions from NCs and the formation of secondary phases.
(36) This observation is consistent with the evidence from a study of doped ZnO NCs (ref 10) that the critical nucleus formation excludes the dopant ions which are then incorporated homogeneously as NCs grow.
(37) Dau, H.; Liebisch, P.; Haumann, M. *Anal. Bioanal. Chem.* **2003**, *376*, 562−583.
(38) Sabergharesou, T.; Wang, T.; Ju, L.; Radovanovic, P. V. *Appl. Phys. Lett.* **2013**, *103*, 012401.
(39) (a) Prewitt, C. T.; Shannon, R. D.; Rogers, D. B.; Sleight, A. W. *Inorg. Chem.* **1969**, *8*, 1985−1993. (b) Parent, P.; Dexpert, H.; Tourillon, G.; Grimal, J.-M. *J. Electrochem. Soc.* **1992**, *139*, 276−281. (c) Nadaud, N.; Lequeux, N.; Nanot, M.; Jove, J.; Roisnel, T. *J. Solid State Chem.* **1998**, *135*, 140−148.
(40) Liehr, A. D. *Prog. Inorg. Chem.* **1962**, *3*, 281−314.
(41) McClure, D. S. *J. Chem. Phys.* **1962**, *36*, 2757−2779.
(42) (a) Fackler, J. P., Jr.; Davis, T. S.; Chawla, I. D. *Inorg. Chem.* **1965**, *4*, 130−132. (b) Dingle, R. *Inorg. Chem.* **1965**, *4*, 1287−1290.
(43) Fackler, J. P., Jr.; Chawla, I. D. *Inorg. Chem.* **1964**, *3*, 1130−1134.
(44) Stanek, C. R.; McClellan, K. J.; Uberuaga, B. P.; Sickafus, K. E.; Levy, M. R.; Grimes, R. W. *Phys. Rev. B* **2007**, *75*, 134101.
(45) (a) Eichel, R.-A. *Phys. Chem. Chem. Phys.* **2011**, *13*, 368−384. (b) Las, W. C.; Gouvea, D.; Sano, W. *Solid State Sci.* **1999**, *1*, 331−337.
(46) Coey, J. M. D.; Chambers, S. A. *MRS Bull.* **2008**, *33*, 1053−1058.
(47) Kaspar, T. C.; Heald, S. M.; Wang, C. M.; Bryan, J. D.; Droubay, T.; Shutthanandan, V.; Thevuthasan, S.; McCready, D. E.; Kellock, A. J.; Gamelin, D. R.; Chambers, S. A. *Phys. Rev. Lett.* **2005**, *95*, 217203.
(48) Stohr, J. *J. Magn. Magn. Mater.* **1999**, *200*, 470−497.
(49) (a) Hegde, M.; Farvid, S. S.; Hosein, I. D.; Radovanovic, P. V. *ACS Nano* **2011**, *5*, 6365−6373. (b) Farvid, S. S.; Hegde, M.; Hosein, I. D.; Radovanovic, P. V. *Appl. Phys. Lett.* **2011**, *99*, 222504.
(50) Ju, L.; Sabergharesou, T.; Stamplecoskie, K. G.; Hegde, M.; Wang, T.; Combe, N. A.; Wu, H.; Radovanovic, P. V. *J. Am. Chem. Soc.* **2012**, *134*, 1136−1146.
(51) (a) Philip, J.; Punnoose, A.; Kim, B. I.; Reddy, K. M.; Layne, S.; Holmes, J. O.; Satpati, B.; Leclair, P. R.; Santos, T. S.; Moodera, J. S. *Nat. Mater.* **2006**, *5*, 298−304. (b) Schwartz, D. A.; Gamelin, D. R. *Adv. Mater.* **2004**, *16*, 2115−2119.